

EVALUATION OF UV AEROSOL RETRIEVALS FROM AN OZONE LIDAR

Shi Kuang^{1*}, Bo Wang¹, Michael J. Newchurch¹, Kevin Knupp¹, Paula Tucker¹, Edwin W. Eloranta², Joseph P. Garcia², Ilya Razenkov², John T. Sullivan³, Timothy A. Berkoff⁴, Guillaume Gronoff^{4,5}, Liqiao Lei^{4,6}, Christoph J. Senff^{7,8}, Andrew O. Langford⁷, Thierry Leblanc⁹, Vijay Natraj¹⁰

¹University of Alabama in Huntsville, Huntsville, Alabama, USA

²University of Wisconsin-Madison, Madison, Wisconsin, USA

³NASA Goddard Space Flight Center, Greenbelt, Maryland, USA

⁴NASA Langley Research Center, Hampton, Virginia, USA

⁵Science Systems and Applications Inc., Lanham, Maryland, USA

⁶Universities Space Research Association, Columbia, Maryland, USA

⁷NOAA Earth System Research Laboratory, Boulder, Colorado, USA

⁸Cooperative Institute for Research in Environmental Sciences, University of Colorado, Boulder, Colorado, USA

⁹Jet Propulsion Laboratory, California Institute of Technology, Wrightwood, CA, USA

¹⁰Jet Propulsion Laboratory, California Institute of Technology, Pasadena, California, USA

*Correspondence to: Shi Kuang (kuang@nsstc.uah.edu)

Abstract

Aerosol retrieval using ozone lidars in the ultraviolet spectral region is challenging but necessary for correcting aerosol interference in ozone retrieval and for studying the ozone-aerosol correlations. This study describes the aerosol retrieval algorithm for a tropospheric ozone lidar, quantifies the retrieval error budget, and intercompares the aerosol retrieval products at 299 nm with those at 532 nm from a high spectral resolution lidar (HSRL) and with those at 340 nm from an Aerosol Robotic Network radiometer. After the cloud-contaminated data is filtered out, the aerosol backscatter or extinction coefficients at a 30-m and 10-min resolution retrieved by the ozone lidar are highly correlated with the HSRL products, with a coefficient of 0.95 suggesting that the ozone lidar can reliably measure aerosol structures with high spatio-temporal resolution when the signal-to-noise ratio is sufficient. The actual uncertainties of the aerosol retrieval from the ozone lidar generally agree with our theoretical analysis. The backscatter color ratio (backscatter-related exponent of wavelength dependence) linking the coincident data measured by the two instruments at 299 and 532 nm is 1.34 ± 0.11 while the Ångström (extinction-related) exponent is 1.49 ± 0.16 for a mixture of urban and fire smoke aerosols within the troposphere above Huntsville, AL, USA.

1. Introduction

A tropospheric ozone differential absorption lidar (DIAL) makes measurements of vertical ozone profiles, typically at two wavelengths chosen between 277 and 300 nm with a separation less than 12 nm, by weighing several parameters such as the ozone absorption cross sections, solar background, dynamic range of the detection system, and interference from aerosols and other species (e.g., Alvarez et al., 2011; Browell et al., 1985; De Young et al., 2017; Fukuchi et al.,

001; Kempfer et al., 1994; McDermid et al., 2002; Proffitt and Langford, 1997; Strawbridge et al., 2018; Sullivan et al., 2014). Vertical aerosol profiles are of high interest not only because they are needed for aerosol correction in ozone lidar retrievals (Steinbrecht and Carswell, 1994), but also because simultaneous ozone and aerosol vertical profile measurements provide unique information on their interactions and on sources of pollutant transport (Browell et al., 1994; Langford et al., 2020; Newell et al., 1999). However, there is currently no consensus on the reliability of the aerosol retrievals produced by ozone lidars due to the difficulty of solving the three-component lidar equation and the large variability in aerosol optical properties associated with the multiplicity of aerosol types and size distributions.

The most widely used solution for the elastic single-wavelength aerosol lidar equation is the analytic method developed by Klett (1981). The inversion method then inspired Fernald (1984) to publish a computer algorithm scheme to solve the more general two-component (aerosol and molecular) atmospheric lidar equation. The Klett (1981) inversion requires *a priori* for the lidar ratio (i.e., aerosol extinction-to-backscatter ratio, represented by “*S*” hereafter) to link the aerosol backscatter with its extinction for solving the lidar equation. Lasers used for aerosol lidars are preferred in the visible and infrared bands, typically 532 and 1064 nm for Nd:YAG laser or 694 nm for Ruby laser (Russell et al., 1979), where the ozone absorption is much smaller than molecular and Mie scattering. In the ultraviolet (UV) band for an ozone lidar, the ozone absorption may not be trivial. Some ozone lidars have an aerosol channel available, either independently or sharing receiving optics with the ozone channel (e.g., Browell et al., 1994; De Young et al., 2017; Gronoff et al., 2019; Kovalev and McElroy, 1994; Uchino and Tabata, 1991). For most of the traditional two-wavelength ozone lidars without an aerosol channel, although there has been some discussion about the aerosol retrieval algorithm (e.g., Eisele and Trickl, 2005; Langford et al., 2019; Papayannis et al., 1999; Sullivan et al., 2014), the evaluation of the aerosol retrieval product and its error budget has rarely been addressed. Due to a significant wavelength difference with aerosol lidars, several aspects of the aerosol retrieval using an ozone lidar are worth noting. First, the signal-to-noise ratio (SNR) for ozone lidars decays quicker with altitude due to more significant UV molecular (i.e., Rayleigh) scattering and ozone absorption resulting in a lower retrievable altitude than aerosol lidars. Second, since the molecular and ozone components become more important at UV wavelengths compared to visible and infrared wavelengths, the uncertainties in aerosol retrieval propagated from the calculation of these two components are expected to be larger for ozone lidars than for aerosol lidars. Third, *S* and the wavelength dependence used for the ozone lidar wavelengths may be different from those used for the longer aerosol lidar wavelengths (Ackermann 1998; Eck et al., 1999).

The primary objectives of this article are to investigate the performance of our aerosol retrieval algorithm and to quantify its error budget for the ozone lidar. The secondary goal is to seek the overall wavelength dependence between the aerosol optical properties measured by the ozone lidar at 299 nm and by a high spectral resolution lidar (HSRL) at 532 nm.

2. Instruments and Data Processing

2.1. Ozone Lidar

The Rocket-city Ozone (O_3) Quality Evaluation in the Troposphere (RO_3QET) lidar is located on the campus of the University of Alabama in Huntsville (UAH) at 34.725 °N and 86.645 °W at 206 m asl and is one of the six systems of the Tropospheric Ozone Lidar Network (TOLNet) (<http://www-air.larc.nasa.gov/missions/TOLNet>). This system

74 measures ozone from 0.1 km up to about 12 km during nighttime and up to about 6 km during daytime with a temporal
75 resolution of 2 min. The vertical resolution of the lidar retrievals varies from 150 m in the lower troposphere to 750
76 m in the upper troposphere in order to keep the measurement uncertainty within $\pm 10\%$ (Kuang et al., 2013).

77 The transmitter comprises two Raman-shifted lasers at 289 and 299 nm. Two 30-Hz, 266-nm Nd:YAG lasers
78 pump two 1.8-m Raman cells, respectively, with mixtures of active gas and buffer gas to generate 289 and 299-nm
79 lasers with an average pulse energy of about 5 mJ. The receiving system consists of three receivers with diameters of
80 2.5 cm, 10 cm, and 40 cm, respectively, and four photomultipliers (PMTs) similar to that described by Kuang et al.
81 (2013) except that the solar filters have been replaced by 300-nm short-pass filters for all telescopes. Channels-1, 2,
82 3, 4 represent the 2.5-cm, 10% of the 10-cm, 90% of the 10-cm, and the 40-cm telescope channels, respectively. Since
83 the modification of Channel-4 through the addition of narrow-band solar filters was not completed before the time
84 period of this study, data from this channel was not used in this work, with the net result that uncertainties for ozone
85 retrievals above 6 km during daytime were often too large due to the strong solar background. Lidar signal counting
86 was accomplished by four Licel transient recorders (Licel company, Germany) with both analog and photoncounting
87 (PC) modes, with a sampling rate of 40 MHz corresponding to a 3.75-m fundamental resolution. The cloud base height
88 is determined by the following empirical method. Derivatives of the logarithm of the off-line analog signal are
89 calculated for a lidar signal profile and the first range bin at which the derivative is greater than a certain threshold is
90 considered to be the cloud base height. The threshold is chosen empirically based on the lidar SNR and the vertical
91 resolution. Therefore, lidar data with cloud base lower than 2 km was discarded. The cloud filtering process should
92 be conducted carefully because an elastic lidar without a polarization channel is not capable of accurately
93 distinguishing aerosols and clouds solely through their backscatter properties. Five 2-min lidar data intervals were
94 combined to give a 10-min lidar-signal integration time to improve the SNR. Further, six of the 3.75-m fundamental
95 bins were integrated for all channels. In addition, dead-time correction (for PC signal only), background correction,
96 analog-PC signal merging, and signal-induced noise correction were performed.

97 **2.2. Aerosol Retrieval and Uncertainty Estimation**

98 The aerosol profiles were retrieved with an iterative DIAL algorithm. A brief description of this algorithm is provided
99 in this section, with further details in Appendix A. A first-order Savitzky-Golay differentiation filter with a second-
100 degree polynomial was applied to the logarithm of the signal ratios to compute the first-cut ozone profile. This initial
101 ozone profile was substituted back into the three-component lidar equation to derive the profile of aerosol backscatter
102 coefficients at 299 nm by assuming a constant S of 60 sr and boundary value of the aerosol backscatter coefficient at
103 a far-range reference altitude, about 10 km. During the daytime, the ozone retrieval was limited by the lower SNR of
104 the 289-nm channel, but the 299-nm channel had much better SNR due to lower atmospheric extinction and was able
105 to measure aerosol up to higher altitudes. S has large variability as a function of aerosol characteristics, humidity, and
106 wavelength (Ackermann, 1998; Strawbridge et al., 2018; Mishchenko et al., 1997). The S *a priori* value assumed for
107 this study represents a mix of urban and smoke aerosols during the lidar observations (Ackermann, 1998; Burton et
108 al., 2012; Cattrall et al., 2005; Groß et al., 2013; Müller et al., 2007). The *a priori* is application dependent. In the
109 aerosol retrieval uncertainty discussion in Appendix B, we assume a $\pm 20\%$ uncertainty for S based on an average
110 standard deviation obtained from prior observations (Müller et al., 2007).

111 Molecular backscatter and extinction profiles were computed from local radiosonde data. Then, the aerosol
112 profile was substituted into the lidar equation again to obtain a stable solution, usually within three iterations. This
113 aerosol profile was further employed to calculate the aerosol correction for ozone retrievals using the first-order Taylor
114 approximation (Browell et al., 1985) by assuming a power-law wavelength dependence for the aerosol extinction and
115 choosing an appropriate Ångström exponent. Since this work focuses only on aerosol retrieval, details of the ozone
116 correction will be described in a future article. Finally, the aerosol profiles derived by the three altitude channels were
117 merged into a single profile in the overlapping altitude zones, i.e., 0.5–1 km for Channels-1 and 2 and 1.5–2 km for
118 Channels-2 and 3.

119 The primary uncertainty sources for the aerosol lidar retrievals are the uncertainties in lidar signal
120 measurement, boundary value assumption for aerosol backscatter coefficient, air density measurement, *S a priori*, and
121 ozone profile input. The relative importance of these sources is altitude dependent. In the planetary boundary layer
122 (PBL) where the air is typically turbid, the *S* uncertainty is dominant while other sources are minor (only few percent).
123 The uncertainty of *S* influences the uncertainty of the aerosol backscatter through a complicated relationship. However,
124 the magnitude of the above two uncertainties can be approximately seen to be close. At the far range (higher than 7
125 km), lidar signal detection noise and inaccurate boundary value assumption are important. Influence from both of the
126 above sources, especially the boundary value, on the aerosol retrieval quickly decreases towards the ground from the
127 far range. In the middle range (PBL top – 7 km), both the air density measurement error and lidar signal detection
128 noise are essential. Uncertainty due to ozone profile input is relatively unimportant and is only few percent at most
129 altitudes. Figure B1 presents an example of the aerosol backscatter uncertainty calculated from 10-min nighttime
130 RO₃QET lidar data. The error budget estimate generally justifies the choice of using 6 km as the maximum altitude
131 for RO₃QET-HSRL comparison since the total uncertainty for the RO₃QET aerosol retrieval could be unacceptably
132 large (i.e., persistently larger than 100%).

133 **2.3. HSRL**

134 The University of Wisconsin HSRL (Eloranta, 2005) was deployed in Huntsville, AL from 19 June to 4 November
135 2013 and operated almost 24 hours every day to support the Studies of Emissions and Atmospheric Composition,
136 Clouds and Climate Coupling by Regional Surveys SEAC⁴RS campaign (Kuang et al., 2017). The HSRL transmitter
137 was a diode-pumped Nd:YAG laser at 532 nm with a pulse energy of about 50 μJ and a pulse repetition frequency of
138 4 kHz. The expanded laser beam was transmitted coaxially with a 40-cm telescope with a tiny field of view (FOV) of
139 100 μrad to reduce solar background. The HSRL spectral filtering can separate the molecular backscatter from the
140 aerosol backscatter due to the molecular Doppler broadening effect, while the particulate backscatter remains
141 spectrally unbroadened. Aerosol backscatter coefficients can then be calculated as the difference between the total
142 return and the molecular component (Grund and Eloranta, 1991). In principle, aerosol extinction can be computed by
143 comparing the measured attenuated molecular backscatter to a reference, unattenuated molecular backscatter profile
144 that is calculated from the radiosonde-measured air density profile or a numerical model (Hair et al., 2008). However,
145 small and fast signal fluctuations were found in the partial overlap region (between the surface and about 4.5 km) for
146 the data taken in Huntsville so that aerosol extinction below 4.5 km cannot be derived with satisfying precision. The
147 signal fluctuations were probably caused by small optical misalignments from temperature changes within the lidar

148 system (Reid et al., 2017). The aerosol backscatter calculation is not affected by the lidar signal fluctuations since any
 149 range-dependent instrument effects are canceled out. Therefore, we focus on the aerosol backscatter intercomparison
 150 between the HSRL and RO₃QET. If aerosol extinction is needed for the HSRL, we will calculate it from the aerosol
 151 backscatter by assuming a constant lidar ratio. The HSRL provides aerosol products with a 30-m vertical resolution
 152 and 1-min temporal resolution from near the surface to 15 km. To achieve sufficient SNR for both HSRL and ozone
 153 lidar and to reduce the uncertainty arising from the clock bias of the controlling computers, we adopt 10-min temporal
 154 average and 30-m vertical average for both HSRL and ozone lidar in the intercomparison study. The HSRL has a
 155 backscatter measurement precision better than 10^{-7} (m sr)⁻¹ for a 1-min signal average (Reid et al., 2017), which
 156 represents an estimated precision for the extinction coefficient of better than 2×10^{-6} m⁻¹ for a 10-min average.

157 3. Intercomparison Results

158 We select four time periods (21–23 June, 14–15 August, 27–28 August, and 5–6 September 2013) to investigate the
 159 ozone lidar capability for measuring aerosol column and range-resolved profiles. All four cases have coincident ozone
 160 lidar and HSRL observation periods longer than 24 hours, fully covering the convective mixing layer development
 161 and collapse processes (Klein et al., 2019) and having significant smoke layers in the free troposphere. Due to the
 162 significant extinction and potential multiple scattering caused by clouds, the ozone lidar is incapable of measuring
 163 either ozone or aerosol accurately above clouds, especially thick clouds. Therefore, data contaminated by clouds is
 164 filtered out. At this time, the narrow-band interference filters had not been incorporated into the receiving system, and
 165 the wide-band filter resulted in substantial solar background during the daytime; hence, we set 6 km asl as the
 166 maximum altitude for intercomparison. The uncertainty of the aerosol retrieval owing to lidar signal measurement
 167 error is dominant at far range and is determined by the lidar SNR, as shown in Appendix B.2. The solar background
 168 is an important noise resulting in the lidar signal measurement error during daytime and is partly responsible for the
 169 high aerosol retrieval uncertainty above 6 km as shown by the example in Figure B1. The 10-min HSRL profiles are
 170 interpolated to the times of the ozone lidar data.

171 First, we investigate the correlation of the integrated (or column) aerosol backscatter between the ozone lidar
 172 and HSRL to obtain a general relationship between their averages. Figure 1 shows that the RO₃QET- and HSRL-
 173 derived integrated backscatter coefficients for all four cases are highly correlated, with a Pearson correlation
 174 coefficient of 0.99. The root mean square error (RMSE), the standard deviation of the residuals, is negligibly small at
 175 1×10^{-3} sr⁻¹, suggesting that the linear regression equation can accurately represent the relationship between the AOD
 176 measured by the two instruments. The 493 sampling profiles cover 82 hours of coincident ozone lidar and HSRL
 177 observations. We define the aerosol backscatter color ratio (\mathring{a}_β) as (Burton et al., 2012):

$$178 \quad \mathring{a}_\beta = -\frac{d(\ln\beta_A)}{d(\ln\lambda)} = -\frac{\ln\left(\frac{\beta_A^{299}}{\beta_A^{532}}\right)}{\ln\left(\frac{299}{532}\right)}, \quad (1)$$

179 where β_A^{299} and β_A^{532} represent the aerosol backscatter coefficient at 299 and 532 nm, respectively. The subscript “A”
 180 represents the “aerosol” component, to be distinguished from the “molecular” contribution that is represented by
 181 subscript “M” in the Appendix. \mathring{a}_β is an exponent denoting backscatter-related wavelength dependence, to be
 182 distinguished from the commonly-used Ångström exponent (Ångström, 1929) that refers to the wavelength
 183 dependence of optical thickness or extinction coefficient. \mathring{a}_β is also different from another often-used concept, “color

184 ratio of the lidar ratios”, which refers to the ratio of S at two different wavelengths. The slope of the regression, equal
185 to 2.16, results in the best least-squares fit value of 1.34 for $\hat{\alpha}_\beta$ at 299 and 532 nm. The uncertainty of the column β_A^{299}
186 is expected to be smaller than the uncertainty for β_A^{299} at a particular altitude and for a 10-min integration time (in
187 Figure B1) since the average over longer time and altitude range greatly reduces the random noise as suggested by the
188 small RMSE in Figure 1. If the uncertainty of the column β_A^{299} measurements is estimated to be 20% which is
189 primarily due to the uncertainty of the S *a priori* (a systematic error), we can estimate the corresponding uncertainty
190 for $\hat{\alpha}_\beta=1.34$ to be ± 0.11 by error propagation from Eq. (1). $\hat{\alpha}_\beta$ has important applications in aerosol type classification
191 from (spectral) aerosol lidar measurements (e.g., Cattrall et al., 2005; Hair et al., 2008; Müller et al., 2007). There is
192 significant variation in $\hat{\alpha}_\beta$ for 532–1064 nm reported in different studies, with numbers ranging from negative values
193 to 2.3 (Burton et al., 2012; Cattrall et al., 2005; Müller et al., 2007). However, all of these studies show a larger value
194 of $\hat{\alpha}_\beta$ for smoke and urban aerosols than for maritime and dust aerosols. Since most previous studies report $\hat{\alpha}_\beta$ for
195 wavelengths longer than 355 nm, $\hat{\alpha}_\beta$ calculated in this study for 299–532 nm could provide valuable data for UV
196 wavelengths.

197 In practice, aerosol extinction is a more meaningful parameter and more relevant for several applications than
198 backscatter. For the HSRL, the extinction coefficients are linearly converted from the backscatter coefficients by
199 assuming a constant $S = 55$ sr with 20% uncertainty, in the same manner as Reid et al. (2017). The estimated Ångström
200 exponent for 299 and 532 nm is 1.49 ± 0.16 , using the data in Figure 1 after considering uncertainties in S for both
201 lidars. The calculated Ångström exponent is different from the backscatter-related wavelength exponent because of
202 the wavelength dependence of S . The Ångström exponent from this study (1.49 ± 0.16) is within a reasonable range
203 compared to previous studies. For example, the Ångström exponent was measured by a Raman lidar to be between
204 1.35 ± 0.2 and 1.56 ± 0.2 at 355 nm for smoke aerosols in Canada (Strawbridge et al., 2018). The Ångström exponent
205 for urban aerosols was measured to be 1.4 ± 0.5 in Europe and 1.7 ± 0.5 in North America for 355 and 532 nm (Müller
206 et al., 2007).

207 The Aerosol Robotic Network (AERONET) (Holben et al., 1998) provides aerosol optical depth (AOD)
208 measurements in eight spectral bands between 340 and 1020 nm with a temporal resolution of about 15 min. The
209 measurement uncertainty for AERONET AOD is within 0.02 and is expected to be larger in the UV bands (Eck et al.,
210 1999; Holben et al., 2001). Even though the measurement is at a different wavelength, the AERONET AOD at 340
211 nm can provide an additional constraint for the choice of S for the RO₃QET aerosol retrieval, especially since both
212 instruments are at the same location. Figure 2 presents the intercomparison of the RO₃QET lidar derived AOD at 299
213 nm and all available AOD data at 340 nm (Smirnov et al., 2000) from the collocated AERONET sun-sky radiometer
214 (data for 21–23 June is unavailable). The near-surface region is assumed to be homogeneous and assigned the same
215 aerosol extinction values as the lowest available 30-m layer from the RO₃QET retrievals. Then, the aerosol extinction
216 coefficients are integrated from 0 to 6 km asl to calculate the lidar-derived AOD. The omission of aerosol extinction
217 above 6 km and the homogeneity assumption for the near-surface region are sources of bias for the comparison since
218 the AERONET instrument measures the total column AOD. The lidar has more data and higher temporal resolution,
219 therefore, the lidar-derived AOD is interpolated to the AERONET measurement times. Figure 2 shows that the AOD
220 retrieved by the two instruments has a correlation coefficient of 0.97 and a small RMSE for a total duration of about

221 31 hours. The mean percentage difference between the RO₃QET and AERONET AOD is 15±9%. The *S a priori*
222 directly affects the AOD calculation. The lidar-derived AOD is on average 15% larger than the AERONET AOD due
223 to the shorter wavelength of the lidar measurement, suggesting that the choice of $S = 60$ sr is appropriate. For a rough
224 estimation, the 1- σ standard deviation (9%) of the differences can be considered as the uncertainty of S if the variability
225 of these differences are mostly due to the variation in S . Considering that AERONET measures the column average
226 AOD, with longer temporal integration, has its own uncertainty, and covers only 38% of the total observational period,
227 our assumption for $S = 60 \pm 20\%$ sr is appropriate for RO₃QET lidar profiling measurements with higher temporal and
228 vertical resolution and should be good enough to cover various uncertainty sources. The collocated AERONET data
229 enhances the credibility of our lidar aerosol retrieval and help evaluate the *S a priori*, with the caveat that the 124
230 paired data covering 31 hours is not a large sample. We do not show HSRL-AERONET comparison here since Reid
231 et al. (2017) have done so using more extensive data in a visible band taken at the UAH site in summer 2013.

232 Figure 3 presents the intercomparison of the aerosol backscatter retrieved by the HSRL and the RO₃QET
233 lidar for the four cases in 2013. The HSRL-derived aerosol backscatter coefficients are scaled to 299 nm (represented
234 by “HSRL-converted” hereafter) using the best-fit exponent value $\hat{\alpha}_\beta = 1.34$. Some clouds lower than 2 km show up in
235 the HSRL curtains but not in the RO₃QET curtains (e. g., 1500–2100 on 15 August and 1500–2100 on 28 August).
236 These low-cloud-contaminated data were discarded in the RO₃QET lidar pre-processing program since the ozone lidar
237 probes the atmosphere with a shorter wavelength than the HSRL, and is, therefore, more affected by cloud interference.
238 Profiles with clouds higher than 2 km measured by the RO₃QET were retained, and the aerosol retrievals below the
239 clouds were used for the range-resolving intercomparisons.

240 In terms of the aerosol measurement evaluation, we pay attention to the two capabilities of the RO₃QET lidar:
241 measuring the PBL diurnal evolution and measuring free-tropospheric smoke layers. In Figure 3, the PBL heights
242 measured by the two lidars, which are identified by large aerosol gradients, are highly consistent for all cases. The
243 development of the convective mixing layer in the early morning, an important process responsible for surface ozone
244 increase, can be visually identified in most RO₃QET curtains (e.g., 1400–1700 UTC or 0900–1200 local time in Figure
245 3-h). The aerosol structures and evolution in the free troposphere measured by the RO₃QET lidar are highly similar to
246 those measured by the HSRL. For example, the RO₃QET lidar captured an extremely thin aerosol layer at ~5-km
247 altitude on 27–28 August (Figure 3-g), which probably originated from the Pacific Northwest fire and has been
248 discussed by Reid et al. (2017). The large aerosol uncertainties for the RO₃QET lidar at far ranges are consistent with
249 expectation. As demonstrated in Appendix B, aerosol retrieval uncertainties due to lidar signal measurement error and
250 the boundary value chosen at the reference altitude, two of the most important sources of uncertainty, increase with
251 altitude and may exceed 100% at ~7 km.

252 To evaluate the range-resolving capability of the ozone lidar for aerosol retrieval, we intercompared the
253 aerosol backscatter coefficients, for all cases, from the two instruments with a 10-min temporal resolution and a 30-
254 m vertical resolution after filtering out cloud-contaminated data, as shown in Figure 4. The high correlation coefficient
255 of 0.95 suggests that the RO₃QET lidar can capture the aerosol variability with high spatio-temporal resolution. The
256 correlation coefficient (0.95) between the two high vertical resolution retrievals is slightly lower than that between the
257 RO₃QET and column-averaged HSRL retrievals (0.99, see Figure 1) due to less vertical average. The HSRL-converted

258 backscatter is calculated using $\hat{\alpha}_\beta=1.34$ and the regression equation in Figure 1. We expect the slope of the data in
259 Figure 4 to be very close to 1. However, the actual slope is 1.08, reflecting the fact that there are a large fraction of
260 points with small aerosol backscatter and larger residuals in clean air (low aerosol) regions. This is not surprising since
261 the HSRL has higher measurement precision than the RO₃QET lidar so that their relative differences in clean air
262 regions can be large.

263 Figure 5 presents the mean and 1- σ standard deviations of the relative differences between RO₃QET and
264 HSRL retrievals, $(\text{RO}_3\text{QET}-\text{HSRL})/\text{HSRL}$, to be compared with the theoretical 1- σ error calculated as outlined in
265 Appendix B. The HSRL measurements are considered as the “true” values to be compared with the RO₃QET
266 measurements. Both the theoretical and actual 1- σ values generally increase with altitude. The actual differences
267 between RO₃QET and HSRL measurements are mostly within or of comparable order of magnitude to the theoretical
268 calculation of the RO₃QET measurement uncertainties. The structures of the theoretical uncertainties are consistent
269 with the actual differences at most altitudes, with few exceptions. For example, the large discrepancies (red lines
270 compared to blue lines in Figure 5) occurring at ~ 4.5 km in Figure 5 (c) and ~ 1.5 km in Figure 5 (d) are primarily
271 because of small number division effects for the extremely clean atmospheric layers (also see Figure 3). Aerosol
272 backscatter of clean air can be accurately measured by the HSRL, but may be beyond the measurement sensitivity of
273 RO₃QET.

274 In Figure 5, the RO₃QET-measured aerosols are generally higher than the HSRL-measured aerosols between
275 5 and 6 km so that the RO₃QET-HSRL differences are biased to positive altitude values. These positive biases can be
276 caused by two reasons. First, the RO₃QET derived aerosol extinction above 5 km is obviously larger than that from
277 HSRL during daytime due to the solar background impact, which is especially strong in the summer. The relative
278 differences are even worse in clean (compared to turbid) regions during the daytime because of the small number
279 division effect mentioned earlier. It can be seen from Figure 3 that RO₃QET nighttime retrievals above 5 km and
280 daytime retrievals below 5 km are relatively good due to either lower solar background or larger lidar signal resulting
281 in better SNR. There were both clean and smoky layers between 5 and 6 km for the four cases; therefore, the positive
282 differences cannot be explained solely by the lower capability of RO₃QET for measuring clean air. We hypothesize
283 that another reason causing the positive differences between 5 and 6 km is the underestimated backscatter color ratio
284 for the smoke aerosols. We converted the HSRL backscatter from 532 to 299 nm using a constant backscatter color
285 ratio, 1.34, which represents an average for the column-integrated backscatter. The most significant contribution to
286 integrated backscatter comes from PBL aerosols, which are mostly urban aerosols with a lower backscatter color ratio
287 than either fresh or aged smoke (Burton et al., 2012; Cattrall et al., 2005). The uncertainty of the backscatter color
288 ratio was not considered in the error budget of the aerosol retrieval. In addition, we ignored the measurement
289 uncertainty of the HSRL. Therefore, the general agreement of theoretical estimates of aerosol retrieval uncertainties
290 and the actual errors suggests that our analysis of the uncertainty sources in Appendix B is reasonable.

291 **4. Conclusions**

292 We have evaluated the aerosol retrievals at 299 nm from the RO₃QET ozone lidar using both aerosol retrievals at 532
293 nm from the University of Wisconsin HSRL and AERONET AOD data at 340 nm from coincident observations at
294 Huntsville, AL in 2013. The integrated backscatter coefficients below 6 km asl from RO₃QET and HSRL are highly

295 correlated, with a Pearson coefficient of 0.99 after excluding cloud-contaminated data. The aerosol profiles of
 296 backscatter coefficients at 30-m vertical and 10-min temporal resolution retrieved by RO₃QET are also highly
 297 correlated with those from the HSRL with a coefficient of 0.95 suggesting that the ozone lidar is capable of providing
 298 reliable aerosol structure information at high spatio-temporal resolution. Intercomparison of the backscatter product
 299 was performed to avoid additional uncertainty caused by the lidar ratio (S) assumption needed for the HSRL aerosol
 300 extinction retrieval. The RO₃QET-measured AOD below 6 km asl is also highly correlated with the AERONET-
 301 measured AOD, with a correlation coefficient of 0.97. The 340-nm band of the AERONET AOD data is closest to the
 302 ozone lidar wavelength among the available instruments and can, therefore, provide a constraint for the S assumption
 303 for the ozone lidar. Analysis of the intercomparison of AERONET and RO₃QET data confirms that our choice of $S =$
 304 60 sr at 299 nm is appropriate. The aerosol retrieval algorithm and its error budget are shown in the Appendix.
 305 The primary uncertainty sources for the aerosol lidar retrieval are errors in lidar signal measurement, boundary value
 306 assumption, air density calculation, *S a priori*, and ozone profile input. The uncertainty in S assumption is a dominant
 307 source at near range, while the lidar signal measurement and boundary value errors dominate at far range, as shown
 308 in Figure B1 for a sample scenario. Within the middle range (PBL top – about 7 km), the air density calculation error
 309 is essential and is larger or comparable to the lidar signal measurement error. The total uncertainty generally increases
 310 with altitude from about 15% in the PBL to consistently higher than 100% above 7 km. Theoretical estimates of the
 311 error budget are generally consistent with RO₃QET-HSRL measurement differences.

312 By assuming a constant S of 60 sr at 299 nm, the backscatter coefficients measured by RO₃QET and HSRL
 313 are related by a backscatter color ratio (backscatter-related exponent) of 1.34 ± 0.11 for 299 and 532 nm. The extinction-
 314 related Ångström exponent, which is more relevant for various applications, is estimated to be 1.49 ± 0.16 by assuming
 315 $S = 55$ sr for the HSRL at 532 nm. These exponents represent a summertime average for a mixture of urban pollution
 316 and fire smoke. Separation of aerosol types was not done in this work, although we recognize that S and Ångström
 317 exponent vary with the aerosol phase function and size distribution. Aerosol correction for ozone lidar retrievals will
 318 be described in a subsequent paper.

319

320 **Appendix A. Aerosol retrieval algorithm**

321 The ozone DIAL solution can be written as follows:

$$322 \quad n_{(r)} = \frac{-1}{2\Delta\sigma} \times \frac{d}{dr} \left[\ln \frac{P_{\text{on}(r)}}{P_{\text{off}(r)}} \right] + [B] + [E], \quad (\text{A1})$$

323 where $n_{(r)}$ is the ozone number density at range r ; $\Delta\sigma$ is the differential ozone absorption cross section; $P_{\text{on}(r)}$ and $P_{\text{off}(r)}$
 324 are the backscattered on-line and off-line lidar returns; and $[B]$ and $[E]$ represent the differential backscatter and
 325 extinction terms (Browell et al., 1985), respectively, including both molecular and aerosol components. The first term
 326 of the right side of Eq. (A1) is often called the signal term. The subscripts “on” and “off” represent 289 and 299 nm
 327 in this study. The aerosol extinction coefficients at 299 nm are calculated using the following procedure.

328 1) A first-order Savitzky-Golay differentiation filter with a second-degree polynomial and variable fitting
 329 window widths are applied on $\ln \frac{P_{\text{on}(r)}}{P_{\text{off}(r)}}$ to compute the signal term. This smoothing method can accommodate the

330 rapid decay of the lidar signal with altitude to provide sufficient SNR for ozone retrievals by appropriate selection of
 331 smoothing window widths (Leblanc et al., 2016a).

332 2) By canceling the lidar constant using the two lidar equations at range r and $r+\Delta r$ for 299 nm, the aerosol
 333 backscatter coefficients at range r can be expressed as (Uchino et al., 1980):

$$334 \beta_A(r) = -\beta_M(r) + \frac{Z(r)}{Z(r+\Delta r)} [\beta_A(r+\Delta r) + \beta_M(r+\Delta r)] \exp \left\{ -2\Delta r \left[\alpha_A \left(r + \frac{\Delta r}{2} \right) + \alpha_M \left(r + \frac{\Delta r}{2} \right) + \alpha_{O_3} \left(r + \frac{\Delta r}{2} \right) \right] \right\} ,$$

335 (A2)

336 where $\beta_A(r)$ and $\beta_M(r)$ are aerosol and molecular backscatter coefficients at range r , respectively; $Z(r) = P_{\text{off}} r^2$ is
 337 the range-corrected lidar signal at 299 nm; $\alpha_A(r+\Delta r/2)$, $\alpha_M(r+\Delta r/2)$, and $\alpha_{O_3}(r+\Delta r/2)$ represent the average aerosol,
 338 molecular, and ozone extinction coefficients between range r and $r+\Delta r$, respectively. Assuming the 299-nm lidar ratio,
 339 $S = \alpha_A/\beta_A$, is constant with the range at 60 sr for this study and further assuming:

$$340 \alpha_A \left(r + \frac{\Delta r}{2} \right) \approx \alpha_A(r+\Delta r) = S\beta_A(r+\Delta r), \quad (\text{A3})$$

341 Eq. (A2) contains only two unknown variables: the aerosol backscatter coefficient $\beta_A(r+\Delta r)$ and ozone extinction
 342 coefficient $\alpha_{O_3}(r+\Delta r/2)$, which requires knowledge of the ozone number density $n_{(r+\Delta r/2)}$. Molecular backscatter and
 343 extinction can be computed from nearby radiosonde data or a model with acceptable accuracy. For the first iteration
 344 step, $n_{(r+\Delta r/2)}$ can be computed from the signal term in Eq. (A1). By assuming a start value $\beta_A(\text{ref})$ at a reference
 345 range and a constant S with range, $\beta_A(r)$ can be solved by Equation (A2). Then, the first $\beta_A(r)$ profile is substituted
 346 back into (A2) to compute the second estimate by using a more accurate form for $\alpha_A(r+\Delta r/2)$ as:

$$347 \alpha_A \left(r + \frac{\Delta r}{2} \right) = S[\beta_A(r+\Delta r) + \beta'_A(r)]/2, \quad (\text{A4})$$

348 where $\beta'_A(r)$ represents the value from the first estimate. Typically, a stable solution for $\beta_A(r)$, which does not change
 349 significantly from one iteration step to the next, can be obtained with only three iterations of Eq. (A2) and (A4).

350 3) The correction terms, $[B]$ and $[E]$, in Eq. (A1) are calculated by the Browell et al. (1985) approximation,
 351 assuming a power-law dependence with wavelength for the aerosol extinction and choosing an appropriate Ångström
 352 exponent. Since this paper focuses only on aerosol retrievals, the details of the ozone corrections will be described in
 353 a future article.

354 4) Aerosol profiles computed for the three altitude channels are finally merged to a single profile in their
 355 overlapping altitude zones, 0.5–1 km for Channels-1 and 2, 1.5–2 km for Channels-2 and 3.

356

357 **Appendix B. Error budget of the aerosol retrieval**

358 Now we investigate five primary error sources affecting each term on the right side of Eq. (A2). In the following
 359 section, we use the notation Δ to represent the absolute uncertainty and δ to represent the relative uncertainty. For a
 360 function Y , derived from several measurement variables x_1, x_2, \dots , the uncertainty in Y can be estimated by the
 361 following expression using the first-order Taylor expansion approximation when these variables are independent
 362 (Taylor, 1997):

$$363 \Delta Y^2 = \left(\Delta x_1 \frac{\partial Y}{\partial x_1} \right)^2 + \left(\Delta x_2 \frac{\partial Y}{\partial x_2} \right)^2 + \dots . \quad (\text{B1})$$

364 **B.1 Lidar signal measurement error**

365 The error source to determine the normalized lidar signal ratio term $\frac{Z(r)}{Z(r+\Delta r)}$ is the lidar signal measurement error, ΔP .
 366 Although ΔP may be due to various processes such as inaccurate dead-time correction, inaccurate background
 367 subtraction, and signal-induced noise, its dominant component is the lidar signal statistical uncertainty (often called
 368 lidar signal detection noise) and is typically assumed to obey a Poisson distribution. Assuming no error in deciding r ,
 369 by using Eq. (A2) and (B1) we obtain the uncertainty of the aerosol backscatter owing to lidar signal measurement
 370 error, $\Delta\beta_A^{sig}(r)$, relative to the total backscatter as:

$$371 \quad \frac{\Delta\beta_A^{sig}(r)}{\beta_A(r)+\beta_M(r)} = \sqrt{[\delta P(r)]^2 + [\delta P(r + \Delta r)]^2}, \quad (B2)$$

372 where $P(r)$ represents lidar signal counts at r after omitting the wavelength subscript (i.e., 299 nm) and $\delta P(r)$ is just
 373 the inverse of SNR. Eq. (B2) means that the uncertainty of the aerosol backscatter coefficient due to lidar signal
 374 measurement is determined by the lidar SNR similarly to other remote sensing detection techniques. Consequently,
 375 its relative uncertainty can be written as:

$$376 \quad \delta\beta_A^{sig}(r) = \left(\frac{1}{B(r)} + 1\right) \sqrt{[\delta P(r)]^2 + [\delta P(r + \Delta r)]^2}, \quad (B3)$$

377 where $B(r) = \beta_A(r)/\beta_M(r)$ is the aerosol-to-molecular backscatter ratio. As expected, $\delta\beta_A^{sig}(r)$ has a reverse relationship
 378 with $\beta_A(r)$ since it is a relative uncertainty. Figure B1 shows an example of the uncertainty budget for a 10-min lidar
 379 data profile. The aerosol retrieval uncertainty due to the lidar signal measurement error generally increases with
 380 altitude primarily because of the rapidly decaying lidar SNR.

381 **B.2 Boundary value error**

382 According to Eq. (A2), the uncertainty of the aerosol backscatter at r , $\beta_A(r)$, can be induced by the uncertainty of the
 383 backscatter at $r + \Delta r$, $\beta_A(r + \Delta r)$, due to the iterative computation method. The error propagation between the
 384 adjacent altitudes can be determined by their partial differential relationship. Using the traditional far-end solution by
 385 assuming that the air is clean at a reference altitude, the aerosol uncertainty due to the inaccurate boundary value
 386 assumption propagates downward based on the following equation:

$$387 \quad \delta\beta_A^{BV}(r) = \delta\beta_A(r + \Delta r) \left[\frac{1 + \frac{1}{B(r)}}{1 + \frac{1}{B(r+\Delta r)}} \right] \{1 - 2S\Delta r\beta_A(r + \Delta r)[1 + \frac{1}{B(r+\Delta r)}]\}. \quad (B4)$$

388 The yellow line in Figure B1 represents the relative uncertainty of backscatter retrieval due to the boundary value
 389 assumption, $\delta\beta_A^{BV}(r)$, when $\delta\beta_A(r_b) = 1000\%$ (i.e., 10 times overestimate at $r_b = 10$ km). Despite a large
 390 overestimate at the reference altitude, $\delta\beta_A^{BV}(r)$ decreases toward the ground, to less than 10% below 5.5 km and less
 391 than 1% below 3.5 km. Simulations demonstrate that $\delta\beta_A^{BV}(r)$ for an underestimation of $\delta\beta_A(r_b)$ (not shown) is better
 392 than that for an overestimation, indicating that the boundary value is preferred at a smaller value. As suggested by Eq.
 393 (B4), $\delta\beta_A^{BV}(r)$ is affected by both S and B . Larger S (if it is correct) results in smaller $\delta\beta_A^{BV}(r)$ and, therefore, aerosol
 394 retrieval errors converge to zero faster. In other words, the smaller the value of S is, the more sensitive the aerosol
 395 retrieval is to the boundary value error. $\delta\beta_A^{BV}(r)$ decreases with an increase of $B(r)$. This means that $\delta\beta_A^{BV}(r)$ is less
 396 affected by the assumed value of $\beta_A(r_b)$ when the aerosol backscatter becomes more important relative to molecular
 397 backscatter, which occurs at longer wavelengths or under turbid air conditions. It is to be noted that $\delta\beta_A(r_b)$ is
 398 between -1 and $+\infty$ so that the distribution of $\delta\beta_A^{BV}(r)$ is asymmetric with the zero axis.

399 In terms of the influence of the boundary value error, we have compared our calculation with an analytical
 400 solution proposed by Kovalev and Moosmüller (1994) (not shown); the results are almost identical. Aerosol retrieval
 401 uncertainty due to incorrect boundary value assumption tends to converge to zero towards the lidar. It is negligible at
 402 lower altitudes, especially in the PBL, when the air is turbid.

403 B.3 Air density error

404 According to Eq. (A2), the air density profile affects $\beta_M(r)$, $\beta_M(r+\Delta r)$, and the optical depth (or transmittance).
 405 Similarly, we can derive the relative uncertainty in aerosol backscatter owing to the uncertainty in the air density
 406 profile as:

$$407 \delta\beta_A^{AD}(r) = \sqrt{\left\{ \frac{\delta\beta_M(r)}{B(r)} [1 + S_m\Delta r\beta_A(r) + S_m\Delta r\beta_M(r)] \right\}^2 + \left\{ \frac{\delta\beta_M(r+\Delta r) \left[\frac{1}{B(r)} + 1 \right]}{B(r+\Delta r) + 1} [1 - S_m\Delta r\beta_A(r+\Delta r) - S_m\Delta r\beta_M(r+\Delta r)] \right\}^2}$$

408
 409 . (B5)

410 S_m represents the molecular extinction-to-backscatter ratio, which is a constant ($8\pi/3$). The two parts in the square root
 411 are the components due to the uncertainties at r and $r+\Delta r$, respectively. Each component includes the influences from
 412 both molecular backscatter and optical depth. When Δr is small, the contribution of the optical depth error is much
 413 smaller than that of the molecular backscatter error so that (B4) can be approximated as:

$$414 \delta\beta_A^{AD}(r) \approx \sqrt{2} \frac{\delta\beta_M(r)}{B(r)}. \quad (B6)$$

415 It is to be noted that $\Delta\beta_M(r)$ and $\Delta\beta_M(r+\Delta r)$ are independent errors as assumed in Eq. (B1). If they are correlated, Eq.
 416 (B5) will partly cancel out with their covariance term, which is not shown in (B1). Due to the nature of the iterative
 417 computation method, $\delta\beta_A^{AD}(r+\Delta r)$ affects $\delta\beta_A^{AD}(r)$ as noted in Eq. (B4), so that the aerosol retrieval uncertainty due
 418 to air density error will propagate downward. However, model simulation suggests that the systematic error of the air
 419 density calculation has little impact on the aerosol retrieval because of the cancelation of the effect at r and $r+\Delta r$. Eq.
 420 (B6) means the uncertainty in the calculation of molecular backscatter will mostly linearly propagate to aerosol
 421 backscatter. If the 2- σ precision of a radiosonde is 0.3 K and 0.5 hPa for temperature and pressure measurements
 422 (Hurst et al., 2011), the propagated uncertainty onto molecular backscatter is only about 0.1%. However, the real
 423 disturbance of an atmosphere deviating from the actual air density profile may be more significant since there are
 424 usually only a few radiosonde profiles available every day. Hence, we assume $\delta\beta_M(r)$ to be 1%, and the resulting
 425 aerosol retrieval uncertainty is represented by the green line in Figure B1. $\delta\beta_A^{AD}(r)$ can be tens of percent in the free
 426 troposphere and is an important error source for aerosol retrievals (Russell et al., 1979). $\delta\beta_A^{AD}(r)$ is less than 10% in
 427 the PBL because of more turbid air in that region. Since $\delta\beta_M(r)$ is assumed to be a constant in this example, the
 428 variation of $\delta\beta_A^{AD}(r)$ is mostly a result of varying $B(r)$, the aerosol-to-molecular backscatter ratio. Since $B(r)$ generally
 429 increases with an increase in wavelength, $\delta\beta_A^{AD}(r)$ is expected to be smaller at longer wavelengths. Therefore, the
 430 aerosol retrieval is less sensitive to the air density error at longer wavelengths.

431 B.4 Lidar ratio error

432 By using Eqn. (A2) and (B1), the relative uncertainty in aerosol backscatter due to incorrect lidar ratio (S) assumption
 433 can be calculated as follows:

434
$$\delta\beta_A^S(r) = 2 \left[\frac{1}{B(r)} + 1 \right] \Delta S \beta_A(r) \Delta r. \quad (\text{B7})$$

435 $\delta\beta_A^S(r)$ due to ΔS at only range r appears to be small, about 1%, when Δr is specified at 22.5 m. However, ΔS varying
 436 with altitude is mostly systematic and, therefore, $\delta\beta_A^S(r)$ at every altitude will propagate downward, and these effects
 437 will accumulate. The error accumulation is not straightforward to compute as an analytical solution. However, these
 438 effects can be simulated numerically. S is highly variable, and it is difficult to estimate its actual uncertainty range. In
 439 this study, we assume that $\delta S = 20\%$ (or $\Delta S = 12$ sr) according to both previous study (Müller et al., 2007) and the
 440 analysis using the collocated AERONET AOD data at 340 nm. The light-blue line in Figure B1 shows that the
 441 accumulative uncertainties in the aerosol backscatter due to ΔS using Eq. (B7) and (B4) are close to the assumed 20%
 442 uncertainty for δS . $\delta\beta_A^S(r)$ is the largest error source in the PBL which is the near range of the lidar measurement.
 443 $\delta\beta_A^S(r)$ decreases with an increase in wavelength because of increasing $B(r)$. In other words, $\delta\beta_A^S(r)$ is less sensitive
 444 to ΔS at longer wavelengths.

445 **B.5 Ozone error**

446 Similar to S , the ozone uncertainty affects only the transmittance term in Eqn. (A2) and its error propagation on aerosol
 447 backscatter retrieval can be expressed as:

448
$$\delta\beta_A^{O_3}(r) = 2 \left[\frac{1}{B(r)} + 1 \right] \Delta\alpha_{O_3}(r) \Delta r. \quad (\text{B8})$$

449 $\delta\beta_A^{O_3}(r)$ is proportional to the $\left[\frac{1}{B(r)} + 1 \right]$ factor and ozone absorption uncertainty, meaning that $\delta\beta_A^{O_3}(r)$ is smaller at
 450 longer wavelengths due to larger aerosol scattering ratio and smaller ozone absorption. When Δr is specified at 22.5
 451 m, $\delta\beta_A^{O_3}(r)$ is less than 0.3%. We still simulate the vertical accumulation of $\delta\beta_A^{O_3}(r)$ using Eq. (B4). As noted earlier,
 452 the systematic errors of the DIAL ozone measurement tend to accumulate while the random errors tend to cancel out.
 453 The dominant error source for lidar measurements at the far range is typically the lidar signal detection noise, a type
 454 of random error. Therefore, for purposes of estimation, we assume a 5% constant DIAL retrieval uncertainty primarily
 455 covering the uncertainties due to ozone absorption cross section, non-ozone gas interference, and signal saturation
 456 effect (Leblanc et al., 2018; Wang et al., 2017). As shown in Figure B1, the simulated aerosol retrieval uncertainty
 457 due to ozone is relatively minor and is less than 5% at most altitudes.

458 In summary, the uncertainties in aerosol backscatter retrieval for the ozone lidar are controlled by ΔS at near
 459 ranges (i. e., in the PBL) where the air is most turbid and are determined by both the lidar signal detection error and
 460 inaccurate boundary value assumption at far ranges (higher than 7 km) where the air is typically clear. In the middle
 461 range of the lidar measurement (PBL top – 7 km), the air density calculation error may become a significant error
 462 source for aerosol retrieval and may have a comparable influence on the aerosol retrieval as the lidar signal
 463 measurement error. Relative to the above four uncertainty sources, ozone DIAL retrieval error is relatively
 464 unimportant, especially in the lower altitudes where lidar SNR is large enough. All the uncertainty terms are affected
 465 by the aerosol-to-molecular backscatter ratio, $B(r)$, which represents the relative importance of the aerosol component
 466 in both extinction and backscatter processes. Based on the above uncertainty budget analysis, we conclude that the
 467 RO₃QET lidar is capable of measuring aerosol profile reliably below 6 km with the current laser output power.

468

469 **Acknowledgements**

470 The authors thank the Tropospheric Composition Program of the National Aeronautics and Space Administration
471 (NASA)'s Science Mission Directorate for supporting the TOLNet program. A portion of the research was carried out
472 at the Jet Propulsion Laboratory, California Institute of Technology, under a contract with NASA (80NM0018D0004).
473 The views, opinions, and findings contained in this report are those of the authors and should not be construed as an
474 official NASA, National Oceanic and Atmospheric Administration, or U.S. Government position, policy, or decision.
475

476 **Data availability**

477 The ozone lidar data are available at the TOLNet website, <https://www-air.larc.nasa.gov/missions/TOLNet/>. The
478 HSRL data used in this study can be obtained at the University of Wisconsin lidar website, <http://hsrl.ssec.wisc.edu/>.

480 **References**

- 481 Ackermann, J. (1998). The extinction-to-backscatter ratio of tropospheric aerosol: A numerical study. *Journal of*
482 *atmospheric and oceanic technology*, 15(4), 1043-1050.
- 483 Alvarez, R. J., Senff, C. J., Langford, A. O., Weickmann, A. M., Law, D. C., Machol, J. L., ... & Hardesty, R. M.
484 (2011). Development and application of a compact, tunable, solid-state airborne ozone lidar system for
485 boundary layer profiling. *Journal of Atmospheric and Oceanic Technology*, 28(10), 1258-1272.
- 486 Ångström, A. (1929). On the atmospheric transmission of sun radiation and on dust in the air. *Geografiska Annaler*,
487 11(2), 156-166.
- 488 Browell, E. V., Ismail, S., and Shipley, S. T. (1985). Ultraviolet DIAL measurements of O₃ profiles in regions of
489 spatially inhomogeneous aerosols, *Appl. Opt.*, 24(17), 2827-2836.
- 490 Browell, E. V., Fenn, M. A., Butler, C. F., Grant, W. B., Harriss, R. C., & Shipham, M. C. (1994). Ozone and aerosol
491 distributions in the summertime troposphere over Canada. *Journal of Geophysical Research: Atmospheres*,
492 99(D1), 1739-1755.
- 493 Burton, S. P., Ferrare, R. A., Hostetler, C. A., Hair, J. W., Rogers, R. R., Obland, M. D., ... & Froyd, K. D. (2012).
494 Aerosol classification using airborne High Spectral Resolution Lidar measurements—methodology and
495 examples. *Atmospheric Measurement Techniques*, 5(1), 73-98.
- 496 Cattrall, C., Reagan, J., Thome, K., & Dubovik, O. (2005). Variability of aerosol and spectral lidar and backscatter
497 and extinction ratios of key aerosol types derived from selected Aerosol Robotic Network locations. *Journal*
498 *of Geophysical Research: Atmospheres*, 110(D10).
- 499 De Young, R., Carrion, W., Ganoë, R., Pliutau, D., Gronoff, G., Berkoff, T., & Kuang, S. (2017). Langley mobile
500 ozone lidar: ozone and aerosol atmospheric profiling for air quality research. *Applied optics*, 56(3), 721-730.
- 501 Eck, T. F., Holben, B. N., Reid, J. S., Dubovik, O., Smirnov, A., O'Neill, N. T., ... & Kinne, S. (1999). Wavelength
502 dependence of the optical depth of biomass burning, urban, and desert dust aerosols. *Journal of Geophysical*
503 *Research: Atmospheres*, 104(D24), 31333-31349.
- 504 Eisele, H., & Trickl, T. (2005). Improvements of the aerosol algorithm in ozone lidar data processing by use of
505 evolutionary strategies. *Applied optics*, 44(13), 2638-2651.
- 506 Eloranta, E. E. (2005). High spectral resolution lidar. In *Lidar* (pp. 143-163). Springer, New York, NY.

507 Fernald, F. G. (1984). Analysis of atmospheric lidar observations: some comments. *Applied optics*, 23(5), 652-653.

508 Fukuchi, T., Fujii, T., Cao, N., Nemoto, K., & Takeuchi, N. (2001). Tropospheric O₃ measurement by simultaneous
509 differential absorption lidar and null profiling and comparison with sonde measurement. *Optical*
510 *Engineering*, 40.

511 Gronoff, G., Robinson, J., Berkoff, T., Swap, R., Farris, B., Schroeder, J., ... & Adcock, E. E. (2019). A method for
512 quantifying near range point source induced O₃ titration events using Co-located Lidar and Pandora
513 measurements. *Atmospheric Environment*, 204, 43-52.

514 Grund, C. J., & Eloranta, E. W. (1991). University of Wisconsin high spectral resolution lidar. *Optical Engineering*,
515 30(1), 6-13.

516 Groß, S., Esselborn, M., Weinzierl, B., Wirth, M., Fix, A., & Petzold, A. (2013). Aerosol classification by airborne
517 high spectral resolution lidar observations. *Atmospheric chemistry and physics*, 13(5), 2487-2505.

518 Hair, J. W., Hostetler, C. A., Cook, A. L., Harper, D. B., Ferrare, R. A., Mack, T. L., ... & Hovis, F. E. (2008). Airborne
519 high spectral resolution lidar for profiling aerosol optical properties. *Applied optics*, 47(36), 6734-6752.

520 Holben, B. N., Eck, T. F., Slutsker, I. A., Tanre, D., Buis, J. P., Setzer, A., ... & Lavenu, F. (1998). AERONET—A
521 federated instrument network and data archive for aerosol characterization. *Remote sensing of environment*,
522 66(1), 1-16.

523 Holben, B. N., Tanre, D., Smirnov, A., Eck, T. F., Slutsker, I., Abuhassan, N., ... & Kaufman, Y. J. (2001). An
524 emerging ground-based aerosol climatology: Aerosol optical depth from AERONET. *Journal of Geophysical*
525 *Research: Atmospheres*, 106(D11), 12067-12097.

526 Hurst, D. F., Hall, E. G., Jordan, A. F., Miloshevich, L. M., Whiteman, D. N., Leblanc, T., ... & Oltmans, S. J. (2011).
527 Comparisons of temperature, pressure and humidity measurements by balloon-borne radiosondes and frost
528 point hygrometers during MOHAVE-2009. *Atmospheric Measurement Techniques*, 4(12), 2777-2793.

529 Immler, F. (2003). A new algorithm for simultaneous ozone and aerosol retrieval from tropospheric DIAL
530 measurements. *Applied Physics B*, 76(5), 593-596.

531 Kempfer, U., Carnuth, W., Lotz, R., & Trickl, T. (1994). A wide-range ultraviolet lidar system for tropospheric ozone
532 measurements: Development and application. *Review of scientific instruments*, 65(10), 3145-3164.

533 Klein, A., Ravetta, F., Thomas, J. L., Ancellet, G., Augustin, P., Wilson, R., ... & Pelon, J. (2019). Influence of vertical
534 mixing and nighttime transport on surface ozone variability in the morning in Paris and the surrounding
535 region. *Atmospheric environment*, 197, 92-102.

536 Klett, J. D. (1981). Stable analytical inversion solution for processing lidar returns. *Applied optics*, 20(2), 211-220.

537 Klett, James D. "Lidar inversion with variable backscatter/extinction ratios." *Applied optics* 24.11 (1985): 1638-1643.

538 Kovalev, V. A., & Eichinger, W. E. (2004). *Elastic lidar: theory, practice, and analysis methods*. John Wiley & Sons.

539 Kovalev, V. A., & Moosmüller, H. (1994). Distortion of particulate extinction profiles measured with lidar in a two-
540 component atmosphere. *Applied optics*, 33(27), 6499-6507.

541 Kovalev, V. A., & McElroy, J. L. (1994). Differential absorption lidar measurement of vertical ozone profiles in the
542 troposphere that contains aerosol layers with strong backscattering gradients: a simplified version. *Applied*
543 *optics*, 33(36), 8393-8401.

544 Kuang, S., Burris, J. F., Newchurch, M. J., Johnson, S., and Long, S.: Differential Absorption Lidar to Measure
545 Subhourly Variation of Tropospheric Ozone Profiles, *IEEE Transactions on Geoscience and Remote Sensing*,
546 49, 557-571, 10.1109/TGRS.2010.2054834, 2011.

547 Kuang, S., Newchurch, M. J., Burris, J., and Liu, X.: Ground-based lidar for atmospheric boundary layer ozone
548 measurements, *Appl. Opt.*, 52, 3557-3566, 10.1364/AO.52.003557, 2013.

549 Kuang, S., Newchurch, M. J., Johnson, M. S., Wang, L., Burris, J., Pierce, R. B., ... & Warneke, C. (2017).
550 Summertime tropospheric ozone enhancement associated with a cold front passage due to stratosphere-to-
551 troposphere transport and biomass burning: Simultaneous ground-based lidar and airborne measurements.
552 *Journal of Geophysical Research: Atmospheres*, 122(2), 1293-1311.

553 Langford, A. O., Alvarez, I. I., Raul, J., Kirgis, G., Senff, C. J., Caputi, D., ... & McNamara, M. E. (2019).
554 Intercomparison of lidar, aircraft, and surface ozone measurements in the San Joaquin Valley during the
555 California Baseline Ozone Transport Study (CABOTS). *Atmospheric Measurement Techniques*, 12(3), 1889-
556 1904.

557 Langford, A. O., Alvarez, R. J., Brioude, J., Caputi, D., Conley, S. A., Evan, S., ... & Ryoo, J. M. (2020). Ozone
558 production in the Soberanes smoke haze: implications for air quality in the San Joaquin Valley during the
559 California Baseline Ozone Transport Study. *Journal of Geophysical Research: Atmospheres*, 125(11),
560 e2019JD031777.

561 Leblanc, T., Sica, R. J., van Gijsel, J. A. E., Godin-Beekmann, S., Haeefe, A., Trickl, T., Payen, G., and Gabarrot, F.:
562 Proposed standardized definitions for vertical resolution and uncertainty in the NDACC lidar ozone and
563 temperature algorithms – Part 1: Vertical resolution, *Atmos. Meas. Tech.*, 9, 4029-4049, 10.5194/amt-9-
564 4029-2016, 2016a.

565 Leblanc, T., Sica, R.J., Van Gijsel, J.A., Godin-Beekmann, S., Haeefe, A., Trickl, T., Payen, G. and Liberti, G., 2016.
566 Proposed standardized definitions for vertical resolution and uncertainty in the NDACC lidar ozone and
567 temperature algorithms–Part 2: Ozone DIAL uncertainty budget. *Atmospheric Measurement Techniques*,
568 9(8), pp.4051-4078, 2016b.

569 Leblanc, T., Brewer, M. A., Wang, P. S., & Granados Muñoz, M. J. (2018). Validation of the TOLNet lidars: the
570 Southern California Ozone Observation Project (SCOOP). *Atmospheric measurement techniques*, 11, 6137-
571 6162.

572 McDermid, I. S., Beyerle, G., Haner, D. A., & Leblanc, T. (2002). Redesign and improved performance of the
573 tropospheric ozone lidar at the Jet Propulsion Laboratory Table Mountain Facility. *Applied optics*, 41(36),
574 7550-7555.

575 Mishchenko, M. I., Travis, L. D., Kahn, R. A., & West, R. A. (1997). Modeling phase functions for dustlike
576 tropospheric aerosols using a shape mixture of randomly oriented polydisperse spheroids. *Journal of*
577 *Geophysical Research: Atmospheres*, 102(D14), 16831-16847.

578 Müller, D., Ansmann, A., Mattis, I., Tesche, M., Wandinger, U., Althausen, D., & Pisani, G. (2007). Aerosol-type-
579 dependent lidar ratios observed with Raman lidar. *Journal of Geophysical Research: Atmospheres*,
580 112(D16).

581 Newell, R. E., Thouret, V., Cho, J. Y., Stoller, P., Marenco, A., & Smit, H. G. (1999). Ubiquity of quasi-horizontal
582 layers in the troposphere. *Nature*, 398(6725), 316.

583 Papayannis, A. D., Porteneuve, J., Balis, D., Zerefos, C., & Galani, E. (1999). Design of a new DIAL system for
584 tropospheric and lower stratospheric ozone monitoring in Northern Greece. *Physics and Chemistry of the*
585 *Earth, Part C: Solar, Terrestrial & Planetary Science*, 24(5), 439-442.

586 Proffitt, M. H., & Langford, A. O. (1997). Ground-based differential absorption lidar system for day or night
587 measurements of ozone throughout the free troposphere. *Applied optics*, 36(12), 2568-2585.

588 Reid, J. S., Kuehn, R. E., Holz, R. E., Eloranta, E. W., Kaku, K. C., Kuang, S., ... & Atwood, S. A. (2017). Ground-
589 based High Spectral Resolution Lidar observation of aerosol vertical distribution in the summertime
590 Southeast United States. *Journal of Geophysical Research: Atmospheres*, 122(5), 2970-3004.

591 Russell, P. B., Swissler, T. J., & McCormick, M. P. (1979). Methodology for error analysis and simulation of lidar
592 aerosol measurements. *Applied Optics*, 18(22), 3783-3797.

593 Smirnov, A., Holben, B. N., Eck, T. F., Dubovik, O., & Slutsker, I. (2000). Cloud-screening and quality control
594 algorithms for the AERONET database. *Remote sensing of environment*, 73(3), 337-349.

595 Steinbrecht, W., & Carswell, A. I. (1995). Evaluation of the effects of Mount Pinatubo aerosol on differential
596 absorption lidar measurements of stratospheric ozone. *Journal of Geophysical Research: Atmospheres*,
597 100(D1), 1215-1233.

598 Strawbridge, K. B., Travis, M. S., Firanski, B. J., Brook, J. R., Staebler, R., & Leblanc, T. (2018). A fully autonomous
599 ozone, aerosol and nighttime water vapor lidar: a synergistic approach to profiling the atmosphere in the
600 Canadian oil sands region. *Atmospheric Measurement Techniques*, 11(12), 6735-6759.

601 Sullivan, J. T., McGee, T. J., Sumnicht, G. K., Twigg, L. W., & Hoff, R. M. (2014). A mobile differential absorption
602 lidar to measure sub-hourly fluctuation of tropospheric ozone profiles in the Baltimore–Washington, DC
603 region. *Atmospheric Measurement Techniques*, 7(10), 3529-3548.

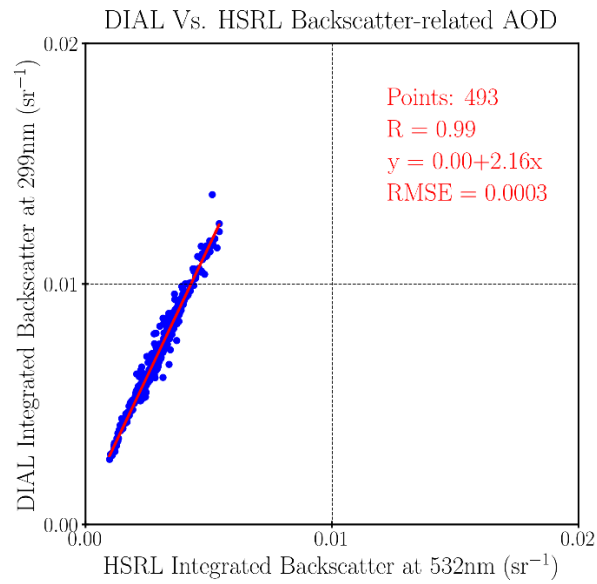
604 Taylor, J. (1997). *Introduction to error analysis, the study of uncertainties in physical measurements*.

605 Uchino, O., Maeda, M., Shibata, T., Hirono, M., & Fujiwara, M. (1980). Measurement of stratospheric vertical ozone
606 distribution with a Xe–Cl lidar; estimated influence of aerosols. *Applied optics*, 19(24), 4175-4181.

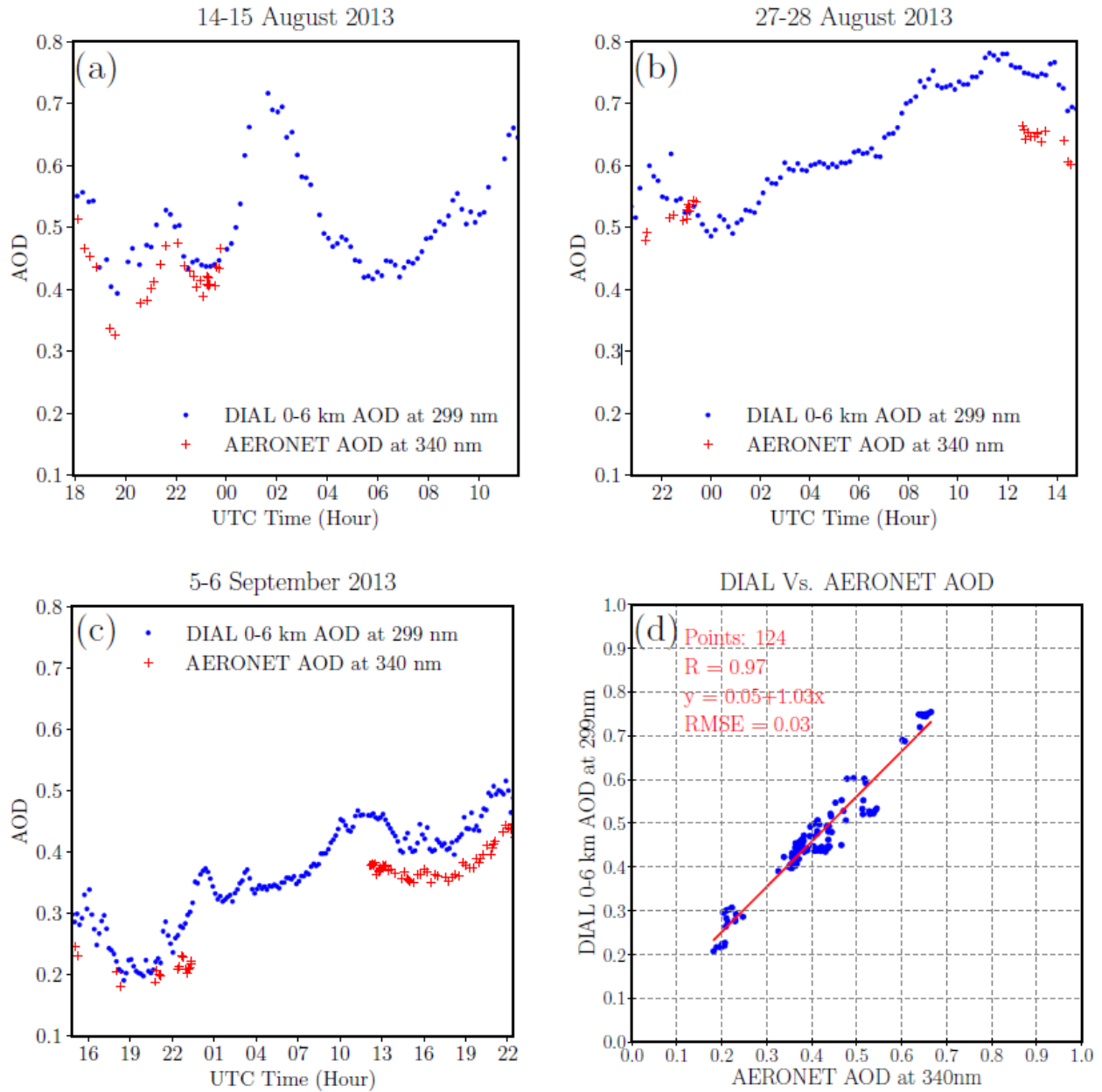
607 Uchino, O., & Tabata, I. (1991). Mobile lidar for simultaneous measurements of ozone, aerosols, and temperature in
608 the stratosphere. *Applied optics*, 30(15), 2005-2012.

609 Wang, L., Newchurch, M. J., Alvarez II, R. J., Berkoff, T. A., Brown, S. S., Carrion, W., DeYoung R. J., Johnson, B.
610 J., Ganoë, R., Gronoff, G., Kirgis G., Kuang, S., Langford, A. O., Leblanc T., McDuffie E. E., McGee, T. J.,
611 Pliutau, D., Senff, C. J., Sullivan, J. T., Sumnicht, G., Twigg, L. W., & Weinheimer, A. J. (2017). Quantifying
612 TOLNet ozone lidar accuracy during the 2014 DISCOVER-AQ and FRAPPE campaigns. *Atmospheric*
613 *Measurement Techniques*, 10(10), 3865-3876.

614

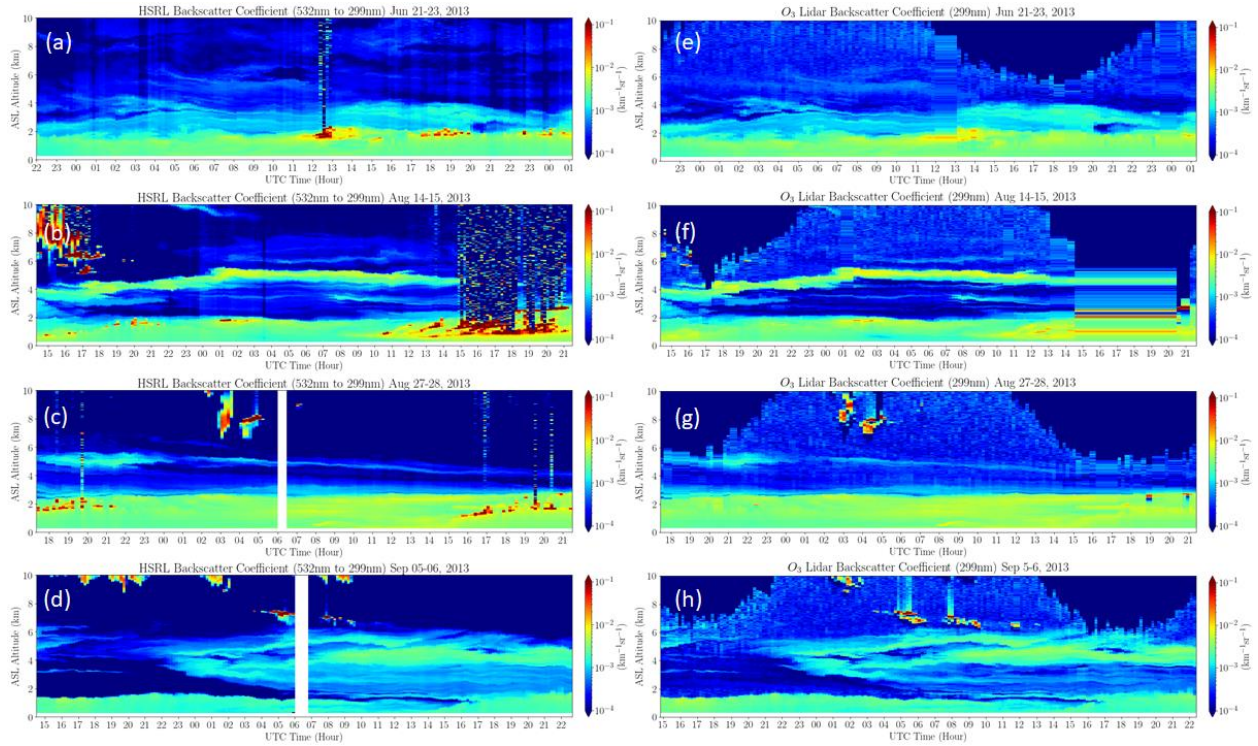


615
 616 Figure 1. Regression of ozone DIAL and HSRL derived integrated aerosol backscatter between 0.4 and 6 km asl using
 617 the best least-squares fit, resulting in a backscatter color ratio of 1.34 for 299–532-nm for four cases in 2013. All the
 618 data was taken at Huntsville, AL, USA, during summer 2013.



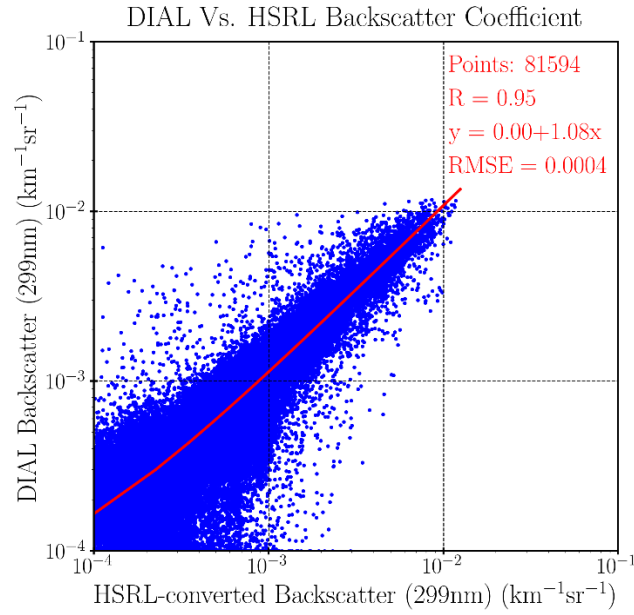
619

620 Figure 2. RO₃QET DIAL derived AOD between 0 and 6 km at 299 nm using $S=60$ sr compared to collocated
 621 AERONET AOD at 340 nm for (a) 14–15 August, (b) 27–28 August, and (c) 5–6 September 2013. (d) Regression of
 622 the paired data after the DIAL AOD is interpolated to the times of AERONET AOD measurements.



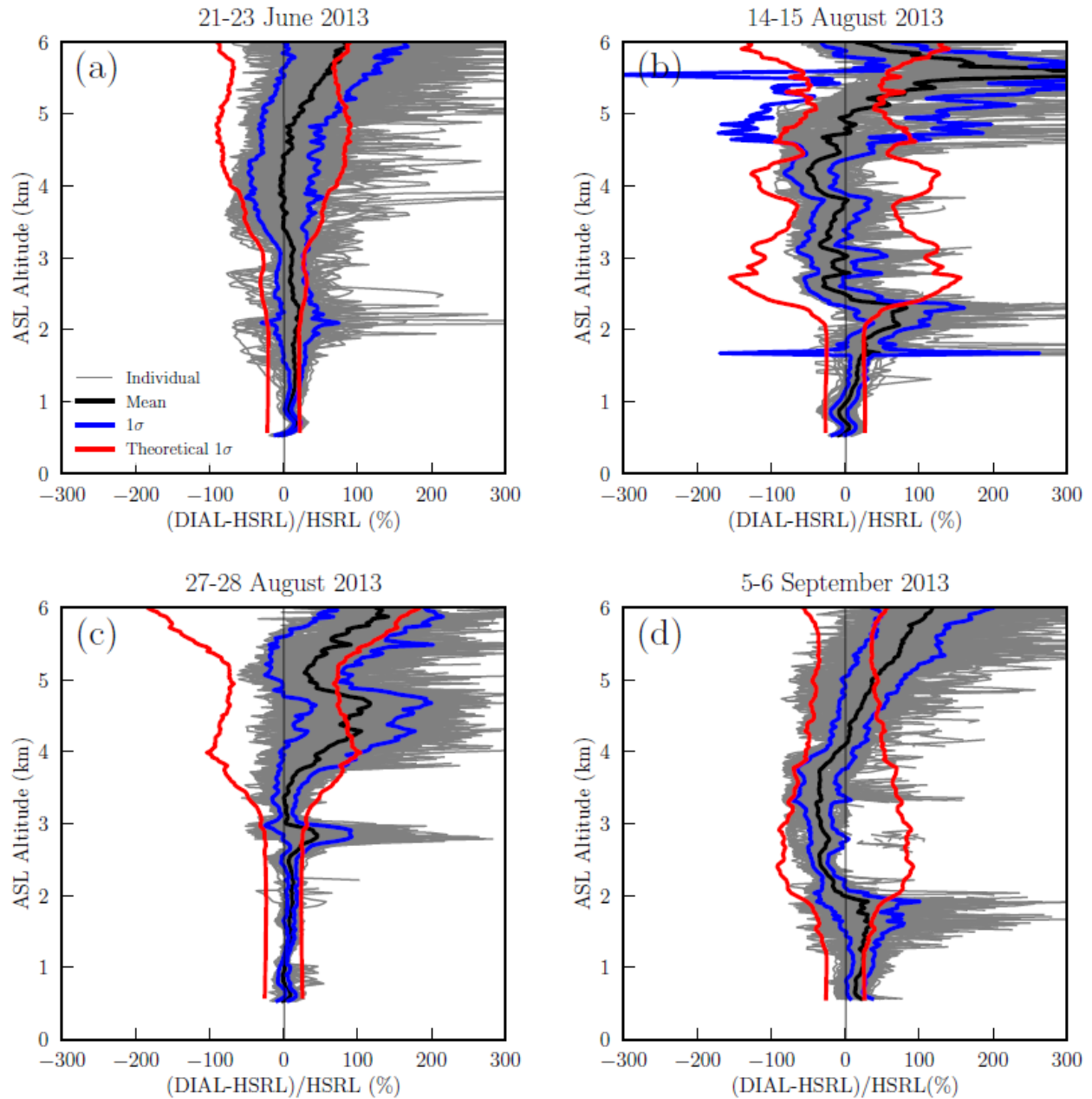
623
 624
 625
 626
 627
 628
 629

Figure 3. HSRL-converted aerosol backscatter coefficients (a, b, c, d) compared to RO₃QET lidar-derived aerosol backscatter coefficients at 299 nm (e, f, g, h), with 10-min temporal resolution and 30-m vertical resolution. The data was taken from 21–23 June (a, e), 14–15 August (b, f), 27–28 August (c, g), and 5–6 September (d, h) 2013. The HSRL-converted aerosol backscatter coefficients are scaled from the original retrievals at 532 nm to 299 nm using Eq. (1) and $\hat{\alpha}_\beta=1.34$.



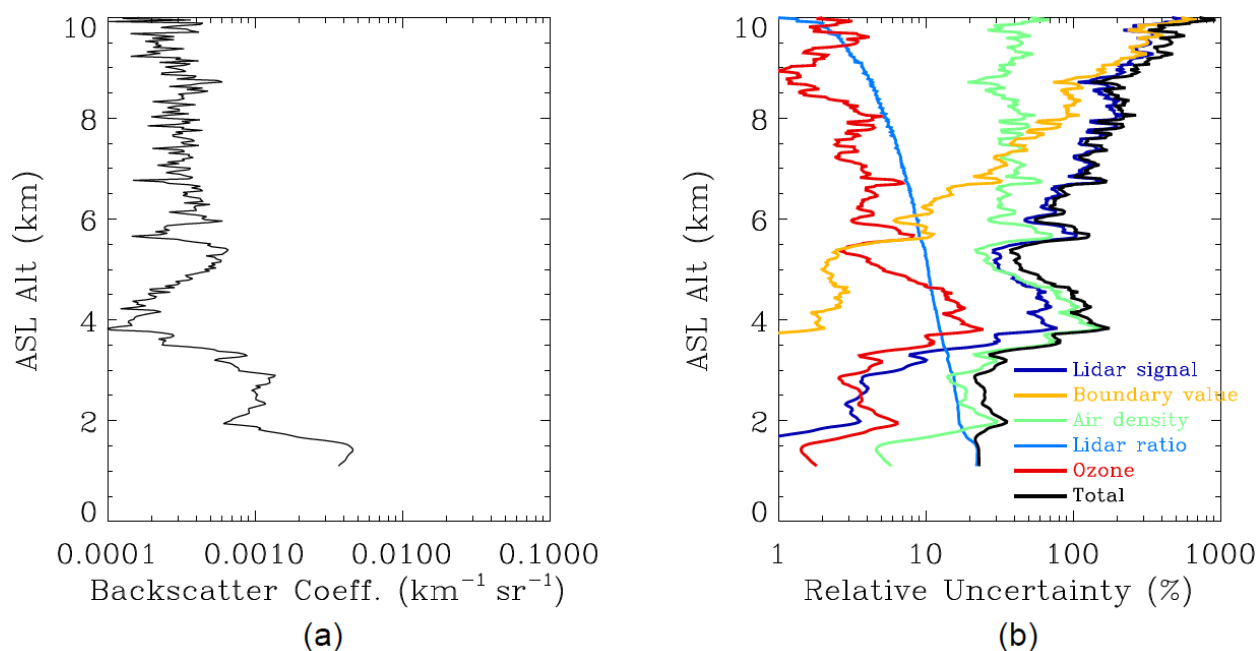
630
631
632
633
634

Figure 4. Regression of ozone lidar measured and HSRL-converted aerosol backscatter coefficients (interpolated to 299 nm with $\hat{a}_\beta=1.34$) with 30-m vertical resolution and 10-min temporal resolution. The regression line is a little curved in the logarithmic scale because the intercept is not exactly zero.



635
 636 Figure 5. Relative differences between RO₃QET and HSRL-converted aerosol backscatter measurements, (RO₃QET-
 637 HSRL)/HSRL, made from (a) 21–23 June, (b) 14–15 August, (c) 27–28 August, and (d) 5–6 September 2013. The
 638 gray and black lines represent the differences for the 10-min individual aerosol backscatter profiles and their mean,
 639 respectively. The blue lines represent the actual 1 σ of the differences compared to the theoretical 1 σ (red lines) of
 640 the RO₃QET lidar aerosol measurement.
 641

642



643

644 Figure B1. An example of (a) aerosol backscatter profile retrieved from 10-min ozone lidar data at about 8:30 UTC
645 on 22 June 2013 and (b) the retrieval error budget for different uncertainty sources. The lidar data was from the
646 Channel-3 receiving system, which covered most of the measurement altitude range, and was arbitrarily chosen for a
647 cloud-free scenario.

648